

All-in-One Sensing System for Online Vibration Monitoring via IR Wireless Communication as Driven by High-Power TENG

Han Wu, Zihan Wang, Boyu Zhu, Hanqing Wang, Chengyue Lu, Meicun Kang, Shenglin Kang, Wenbo Ding,* Lijun Yang, Ruijin Liao, Jiyu Wang,* and Zhong Lin Wang*

Abnormal vibration is a direct response to the mechanical defects of electrical equipment, and requires reliable vibration sensing for health condition evaluation in the associated system. The triboelectric nanogenerator (TENG) triggered by random vibration to generate electrical energy/signal while giving feedback on the vibration state, paving a promising way towards self-powered sensors. Here, an all-in-one sensing system configured with a vibration sensor demonstrates instantaneous discharge boosted TENG and IR wireless communication for vibration state online monitoring. The sandwich-structured TENG combined with mechanical switches can release the co-accumulated charges from dual triboelectric layers to yield giant instantaneous output power of 616 W, which is 10^6 times higher than that of the continuous discharge. Moreover, an IR LED as a transmitter driven by the TENG can form an all-in-one vibration sensor enabling wireless communication, where the sensor can be further integrated with repeaters and phones to establish a wireless vibration online monitoring system for vibration state visualization. This work presents a novel idea to implement high-power TENG with IR communication integration for in situ vibration online monitoring. Such a strategy is potentially available for distributed sensor construction towards abnormal signal monitoring that reflects the operating state of equipment.

1. Introduction

Electric Internet of Things (eIoT) is regarded as the backbone toward future Energy Internet, which has been continuously integrating intelligent sensing, communication technologies, and advanced control strategies to co-serve the smart grid.^[1–5] In most key electrical equipment, where sensor deployment is not only an essential strategy for sensing the operation states of this equipment but also carries critical information about the health conditions.^[6,7] One of the main concerns is the abnormal vibration in equipment caused by intrinsic mechanical defects, whose behavior would be more dangerous under extreme physical environments (wind, rain, lightning, etc.) or shifting electrical parameters (current, electromagnetic, etc.).^[8–10] In this regard, vibration monitoring techniques applied to the key electrical equipment such as a transformer can reflect the mechanical condition of the windings or core, which allows transformer fault prognosis before catastrophic


H. Wu, B. Zhu, H. Wang, M. Kang, S. Kang, L. Yang, R. Liao, J. Wang
State Key Laboratory of Power Transmission Equipment
and System Security and New Technology
Chongqing University
Shapingba, Chongqing 400044, P. R. China
E-mail: jiyuwang@cqu.edu.cn

Z. Wang, C. Lu, W. Ding, J. Wang
Tsinghua-Berkeley Shenzhen Institute
Tsinghua Shenzhen International Graduate School
Tsinghua University
Shenzhen 518055, P. R. China
E-mail: ding.wenbo@sz.tsinghua.edu.cn

Z. L. Wang
Beijing Institute of Nanoenergy and Nanosystems
Chinese Academy of Sciences
Beijing 100083, P. R. China
E-mail: zhong.wang@mse.gatech.edu

Z. L. Wang
CUSPEA Institute of Technology
Wenzhou, Zhejiang 325024, P. R. China

Z. L. Wang
School of Material Science and Engineering
Georgia Institute of Technology
Atlanta, GA 30332, USA

 The ORCID identification number(s) for the author(s) of this article can be found under <https://doi.org/10.1002/aenm.202300051>.

DOI: 10.1002/aenm.202300051

insulation failures.^[11,12] Also, the overhead transmission lines are easily affected by complex meteorological and geographical conditions, where aeolian vibrations are the main observable parameters utilized for state evaluation of fatigues and broken strands.^[13,14] In view of these problems, the abnormal vibrations have attracted noticeable attention in ultrahigh voltage engineering with larger generators, high-capacity transformers, integrated gas-insulated switchgear, and extended-span transmission lines.^[15,16] Hence, vibration state monitoring becomes a necessary tool for these core equipment, which demands vibration sensors to be deployed at each node of power grid for long-term lifecycle work. However, such sensors are even desired to be mounted on the inside of large equipment for reliable detection, thus resulting in difficulties to obtain an in situ continuous power supply, while the electromagnetic interference problem further prevents stable data communication.^[17,18] With the ability of being a promising recyclable power source, the emerging triboelectric nanogenerator (TENG)^[19–21] technology based on the coupling of triboelectrification and electrostatic induction, can convert mechanical vibration energy into electric power to ensure the distributed energy supply. Meanwhile, the variable electrical signals are crucial information in response to the mechanical excitation state. Benefiting from the multistyled structure design and abundant choice of materials, the TENGs exhibit unique merits of light-weight, sustainability, low-cost as well as high voltage and sensitivity.^[22–24] All of these have an enormous advantage to developing a self-powered vibration sensor, simultaneously, the sensor that further integrates advanced communication technology is expected to become an ideal pathway to enable the online vibration state monitoring of the electrical equipment.

So far, the TENG was designed as a sustainable power supply for light-emitting diodes (LEDs), ambient sensors, and low-power-consuming electronics.^[25–27] However, owing to the intrinsic characteristics, TENGs typically produce high voltage and low current outputs with larger impedance (for M Ω -level), which cannot be well matched to the normal electronics with k Ω -level impedance. Zi et al. illustrate that a power management circuit (PMC) plays an essential role as the bridge to provide regulated and efficient power output theoretically, by which they propose a switch circuit strategy to regulate the charge flow in the system to maximize the energy supply efficiency.^[28–30] Among them, introducing silicon controlled rectifier^[31] and metal-oxide-semiconductor field-effect transistor^[32] based electronic switches has achieved excellent output energy. Nevertheless, an external power supply is required to operate the control circuit in the electronic switch, and the electronic components themselves will also incur considerable energy losses. By contrast, the mechanical switch is controlled exactly depending on the travel motion of the TENG to achieve periodic closing and opening, such a straightforward, battery-free, easily integrated method benefits the efficient energy conversion under sustained mechanical excitation.^[33,34] Consequently, the mechanical switch was designed on a sliding TENG that converts continuous discharge (CD) into instantaneous discharge (ID), resulting in a close to zero output impedance, thus the maximum charges are effectively discharged with an external load.^[35] Then, a further endeavor to combine the mechanical switches with opposite-charge-enhancement effect has realized ultrahigh output power,^[36] but the above-mentioned structures

required a large sliding motion for a steady trigger that can hardly be utilized in vibration scenarios. In addition, a contact-separation TENG can work effectively with only mm-level motion, under which the integrated mechanical switches can be easily triggered by such vibration excitation.^[37] Therefore, an advanced mechanical switch triggering mechanism for the contact-separation TENG is promising to be optimized to address the microvibration excitation in engineering applications.

Moreover, a fully self-powered sensor typically involves an extended communication module to realize the information interaction. The mainstream methods are based on traditional radio frequency (RF) technologies, i.e., Bluetooth,^[38] Zigbee,^[39] and RF identification.^[40] However, the integrated modules will consume more energy, which undoubtedly worsens the time for TENG to accumulate energy to operate the module. Besides, by working around the strong electromagnetic field in the complicated ultrahigh voltage electricity scenario, the RF technology will be limited by electromagnetic interference. Prospectively, the optical signal exhibits a superior anti-interference capability owing to its wide bandwidth and short wavelengths.^[41–43] Thus, optical communication shows unique advantages in some regions where RF signals cannot be covered, such as enclosed spaces for electromagnetic shielding effect caused by a metal shell, near-electromagnetic fields, etc. Coupled with features of high speed and high capacity, optical communication has become a powerful supplementary and even alternative to RF technology. Accordingly, a conventional LED is illuminated as a wireless transmitter that can directly transmit information about relevant mechanical stimuli under the excitation of TENG, which is unachievable in an integrated RF module.^[44] Benefiting from the unique capability to deliver real feedback on vibration states, this combination has potential for internal vibration monitoring of equipment without concerns about electromagnetic compatibilities, such as typical scenarios of generator gears and transformer windings, etc. However, the visible light communication system can only work under a really short distance due to propagation loss from the ambient medium. In this case, IR light features a higher penetration rate than visible light, which exhibits favorable properties that are not easily blocked by intermediate mediums.^[45,46] But a large bulk TENG driven by a high-speed rotary motor has realized enough power supply to the IR LED with meter-level communication.^[47] Given the powerful transmission capability, a further optimized portable TENG would be expected to integrate LED for long-distance wireless communication to serve the actual application of vibration monitoring in electrical equipment.

Herein, an all-in-one vibration sensor assembled with instantaneous discharge-boosted TENG and IR wireless communication is proposed for vibration state online monitoring. The TENG was designed as a three-layer sandwich structure with mechanical switches, so that contact occurred between the middle movable layer and the top and bottom fixed layers will be accompanied to trigger the switch on. The opposite triboelectric surfaces were employed on fixed layers to enable co-accumulated charges to be released simultaneously, thus producing enlarged giant instantaneous output. Moreover, such constructed TENG was investigated with triboelectric material and operable vibration space to obtain maximum output and optimum energy conversion efficiency. More importantly, a dual-channel power management circuit was built based on

diodes to realize both DC outputs, whose CD and ID channels co-existed for a wider range of power supply options. Furthermore, an IR LED connected to the ID-channel constructs an all-in-one vibration sensor without additional electronic components, realizing multifunctional features of self-powered, vibration sensing, and wireless communication, which offers the unique advantage of a light-weight size, microvibration triggers, long-distance signal transmission, and antielectromagnetic interference. Finally, the sensor integrated with repeater and mobile phone platform demonstrates a fully wireless vibration online monitoring system, which can be utilized for vibration state visualization over a wide area. This proposed work presents a unique mechanical switch-triggered TENG mode, whose giant ID energy to power IR LED offers a solid path for reliable wireless communication with long distance. The novel concept of an integrated all-in-one sensing system could potentially be utilized in a large-scale power grid that delivers real-time abnormal vibration feedback of electrical equipment for deep health condition analysis.

2. Results and Discussion

2.1. Structure and Working Mechanism

Figure 1a demonstrates the emerging strategy of a fully wireless vibration online monitoring system for the most key electrical equipment in the power grid. The system is composed of an all-in-one vibration sensor cooperated with a user-friendly interface for vibration state monitoring. The vibration sensor simply consists of TENG and IR LED with the function of self-powered sensing and wireless communication. Such a structure renders itself a possibility that to be conveniently deployed on equipment and even in its interior to obtain abnormal vibration information, which is potential for practical application in typical scenarios such as flow excitation in hydraulic turbine instabilities,^[48,49] transformer winding condition assessment,^[50,51] mechanical defect identification for gas-insulated switchgear,^[52,53] and aeolian vibration disrupted transmission line fatigue.^[54,55]

The detailed structural diagram of TENG is illustrated in **Figure 1b**, which is a mechanical switch-integrated three-layer sandwich structure with two couples of contact–separation layers. Specifically, the top and bottom fixed layers are both composed of triboelectric layer with back electrode as well as an independent mechanical contact along one side, and the triboelectric materials herein are polyamide (PA) and polytetrafluoroethylene (PTFE), respectively. While the middle movable layer is a combination of PTFE film and a steel chip with mechanical contacts at one side. Besides, the springs introduced here drive the movable layer to ensure the triboelectric layer is in contact and the mechanical switch is on simultaneously. The sponge is inserted in the fixed layer as a buffer between the electrode and acrylic layer for soft contact and stability. Furthermore, the surfaces of PTFE and PA films were also modified by the plasma etching method to create nanostructure for larger contact areas, and the scanning electron microscope (SEM) images are displayed in the insets of **Figure 1b**. Based on the above-described structure, each component of the TENG was crafted as shown

in **Figure S1** in the Supporting Information. And **Figure 1c** depicts the photograph of the fabricated TENG with overall dimensions of 90 mm × 90 mm × 15 mm (length × width × height) (the fabrication process is described with detail in the Experimental Section).

Figure 2a illustrates the detailed working mechanism of the TENG with mechanical switches in stage (i–iv). For the middle movable layer, the PTFE is combined with PA in top layer, and the steel is combined with PTFE in bottom layer to form a couple of triboelectric layers, respectively. In addition, the two back Cu electrodes are connected to the top and bottom mechanical contacts via an external circuit. Based on a coupled effect of triboelectrification and electrostatic induction,^[56] an equal amount of negative and positive charges will be generated on the surface of triboelectric materials in physical contact. After being separated from each other, the charge transfer occurs between the back electrodes to balance the generated potential difference, as shown in the initial stage (i). According to the electronic affinity of these materials, here we consider the surface charge of PA to be Q_1 , and the PTFE in bottom layer is Q_2 . While the charge quantity of steel is $Q_1 - Q_2$ since it serves as both a triboelectric layer and induction electrode.

As the movable layer approaches the top layer in stage (ii), the charge is driven between the top and bottom electrodes to equalize their potential, until the next stage with maximum charge transfer of $-Q_2$. At stage (iii), the movable layer is in contact with the top layer while the mechanical switch is open via the contacts, where the charge of $Q_1 - Q_2$ in the steel will be released. As the movable layer shifts closer to the bottom layer in stage (iv), the charge is also transferred between the top and bottom electrodes, but with a maximum charge transfer of Q_1 . Back to stage (i), the movable layer finally comes into the original position, and the mechanical switch triggered to open will enable the accumulated charge of $Q_1 - Q_2$ in the bottom electrode to be released into the steel which ensures new electrostatic equilibrium. Theoretically, following the above-described full cycle of the operational process, the total transferred charge quantity of the TENG produces $3(|Q_1| + |Q_2|)$. Compared with conventional contact–separation TENG, a couple of PTFE and PA produces only $2|Q_1|$ in one cycle.

Different from the conventional TENG with CD output, the introduced mechanical switch causes the charge to be transferred as ID output in stages (i) and (iii). Before the switch turns on, the voltage V_{ID} of the external resistance reaches its maximum caused by the accumulated charge, which can be expressed as

$$V_{ID} = \frac{Q_1 - Q_2}{C_T} \quad (1)$$

where C_T is the equivalent capacitance of the TENG with a constant value, which is the PTFE layer at the bottom in stage (i), while stage (iii) represents a serial connection of PTFE and PA layers. When the switch is on, an instantaneous current I_{ID} is generated that can be expressed as

$$I_{ID} = \frac{V_{ID}}{R} e^{-t/\tau} \quad (2)$$

where R is the resistance of the external circuit, τ is the time decay constant, and $\tau = RC_T$. The maximum value of I_{ID} will

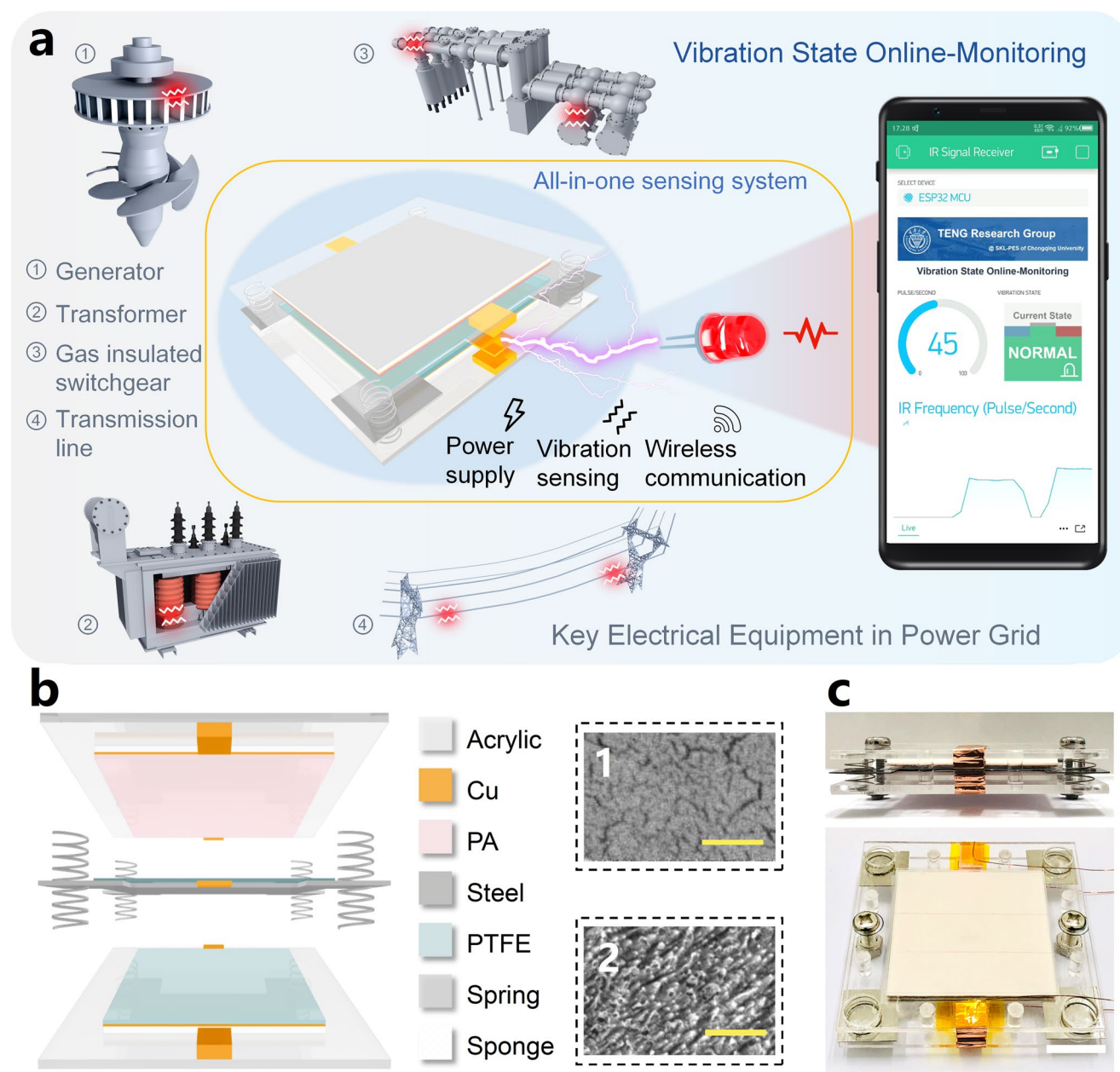


Figure 1. Structural design of the vibration sensor-based fully wireless vibration online monitoring system. a) Schematic illustration of the fully wireless vibration state online-monitoring system based on the all-in-one vibration sensor for the key electrical equipment in power grid. b) Expanded structural composition of the TENG, insets 1 and 2 show the SEM images of the triboelectric layers (scale bar are both: 1 μm). c) Photographs of the fabricated TENG in front view and top view (scale bar: 20 mm).

decay exponentially with time. Thus, the TENG with ID current form can be equated to a series of the voltage source and constant value of C_T , while the equivalent capacitance in conventional TENG is varied continuously under movements (the detailed process is described in Figure S2 in the Supporting Information).

For any external vibration excitations, an alternative contact–separation movement occurs between the movable layer and fixed layers of TENG, and the electricity generation process operates accordingly. The fabricated TENG was driven by a linear motor in a quantified investigation (Figure S3 in the

Supporting Information), and its output current and transferred charge were measured with a load resistance of 100 $\text{M}\Omega$. As shown in Figure 2b,c, the experimental results are well matched with the working mechanism in each stage. The coupling of dual charge accumulation and mechanical switch enables the TENG to exhibit a large peak current and transfer charge in stages (i) and (iii). Consequently, the counted total transferred charge of TENG under one cycle is $\approx 1.2 \mu\text{C}$, nearly three times higher than conventional TENG (Figure S4 in the Supporting Information).

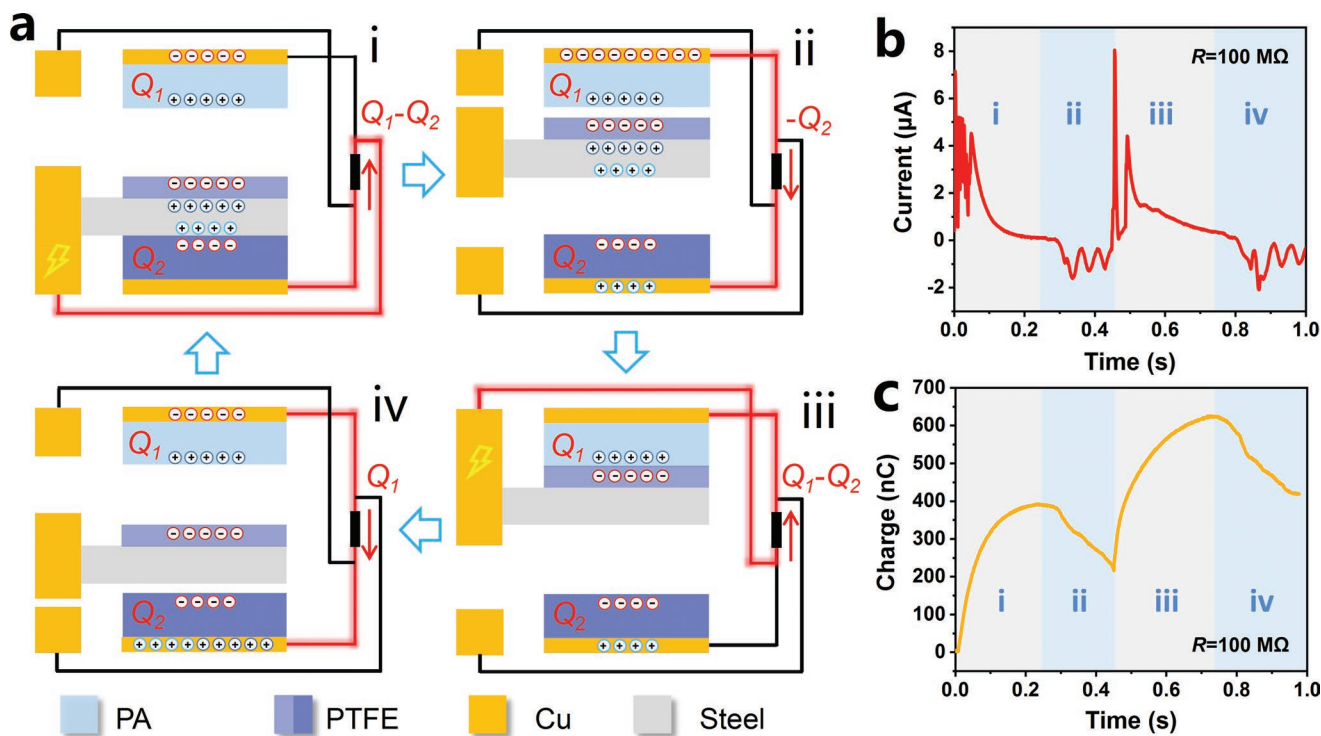


Figure 2. Schematics of the working mechanism of TENG. a) i–iv) Schematic of charge distribution and current direction under a full cycle for a simplified TENG. b) The generated current, and c) the transferred charge of the TENG with an external load resistance of 100 M Ω .

2.2. Output Performance and Characteristics

Figure 3a presents the output current for driving the TENG in one cycle with a smaller external resistance of 1 M Ω , which results in an ID current with a much larger peak value in stages (i) and (iii). In contrast, stages (ii) and (iv) belong to the conventional CD current and still have a little peak value. Among them, the ID current at stage (i) is further observed as shown in the enlarged view of Figure 3b. The phenomenon of multipulse signals happens due to the air breakdown occurring between the mechanical contacts in continuous proximity. Specifically, as the movable layer gradually approaches the bottom layer, the electric field built up by the unbalanced charge exceeds the breakdown electric field will cause the air breakdown between the mechanical contacts. During the first air breakdown, a partial unbalanced charge can be transferred between the bottom electrode and the steel sheet until the unbalanced charge is not sufficient to maintain the electric field strength of the air breakdown voltage. Therefore, a current peak is generated. Subsequently, the movable layer continues to move toward the bottom layer in a certain position, and the newly established electric field once again exceeds the breakdown electric field due to the reduced distance between contacts. Thus, the air breakdown occurs again, in which other parts of the charge transfer will generate a new current peak. After several air breakdowns, the contacts are touched on and all the unbalanced charge is transferred, which makes the charge transfer continuously rather than instantaneously, resulting in a wider waveform than before. Additionally, the amount of transferred charge is obtained by integration of the output current, which remains

consistent with Figure 2c in stage (i). Meanwhile, the voltage–charge (V – Q) plot based on the measured current is graphed in Figure 3c. The output energy E_{out} can be calculated by

$$E_{\text{out}} = \int V dQ \quad (3)$$

From the V – Q plot, a 0.21 mJ output energy in one cycle is obtained. It can be seen that the output energy is mainly delivered in stages (i) and (iii), while stages (ii) and (iv) are almost with invalid output energy.

To further investigate the electrical output performance of TENG, the dependence of the V – Q plot for varied load resistances is shown in Figure 3d. Specifically, the values of E_{out} in ID output remain almost constant with different resistances, which is illustrated in Figure 3e for stage (i), while the values of E_{out} in CD output exhibit a significant gain with higher resistance values, as shown in Figure 3f for stage (ii). Therefore, the E_{out} in CD output should be optimized by applying a matched large load resistance, but ID output will be free.

Besides, the TENG is driven by varied frequencies to further investigate the output characteristics, and the experimental results of the output current with external resistance of 1 M Ω are shown in Figure 3g,h. For conventional CD mode, the output current is highly dependent on frequency because the maximum charge transfer rate is determined by the moving speed, thus resulting in a larger current peak at higher frequencies. As the constant charges of $-Q_2$ and Q_1 are transferred in stages (ii) and (iv), respectively, the peak output current will increase as the drive frequency increases. In contrast, the ID mode profits from the mechanical switch triggered after charge accumulation,

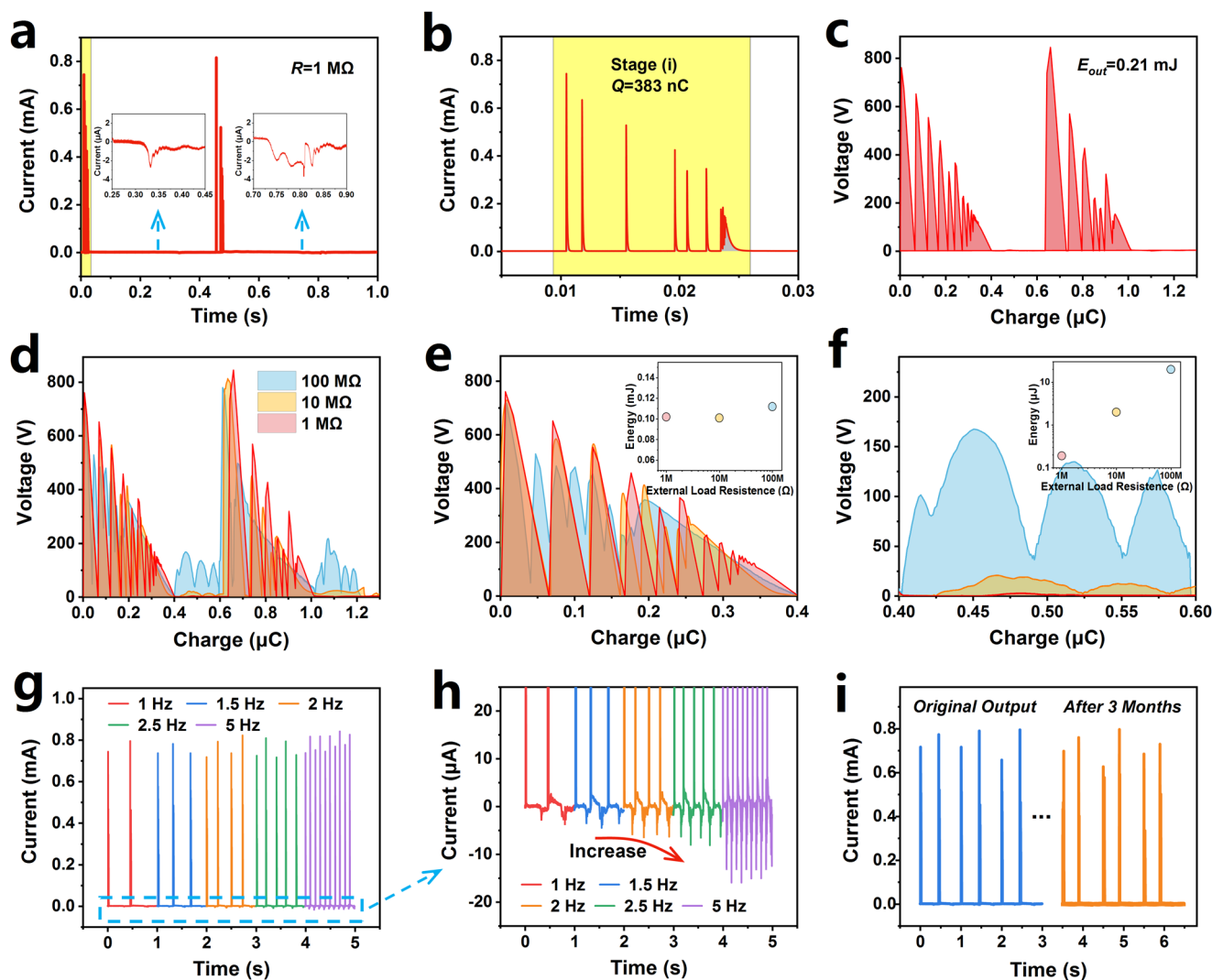


Figure 3. The electrical output performance of the TENG. a) The output current of the TENG with an external load resistance of 1 MΩ and b) the enlarged view in stage (i). c) The V–Q plot of the TENG with an external load resistance of 1 MΩ. d) Dependence of V–Q plot under varied load resistances, and the enlarged view in e) stage (i) and f) stage (iii). g) Dependence of output current under varied frequencies, and the enlarged view h) in stage (ii) and stage (iv). i) Output current comparison between the initial fabricated TENG and the one placed after 3 months.

where the output current is generated only when the contacts reach a fixed position from each other, and all the current in this mode is generated by the discharges between the mechanical contacts. On the other hand, the peak intensity here is attributed to the amount of charge that participated in discharge, which is approximately equal in discharge cycles. Therefore, the ID mode shows a relatively uniform current peak for different frequencies, which is a valuable feature for the energy supply and reliable signal identification in various vibration states.

Additionally, the sustainability of the TENG was also confirmed by a long-term evaluation. After the TENG to be driven 500k cycles and placed in the lab for 3 months, the output remains well constant as shown in Figure 3i. Benefiting from minimum abrasion under the contact–separation mode, the designed TENG demonstrates excellent durability that can be regarded as a favorable characteristic for long-lifetime employment as a distributed sensor.

2.3. Structural Parameters Optimization

Figure 4a shows a “4-Port” method for output charge measurement that has been adopted to validate the opposite-charge-enhanced effect in previous work.^[36] Specifically, the method involves both electrodes and contacts grounded to measure the output charge at the P_1 port, while the transferred charge during stage (i) to stage (iv) is Q_1-Q_2 , $-Q_2$, 0, and Q_1 , respectively (Figure S5 in the Supporting Information). Based on this method, the transferred charge of our designed TENG at P_1 was measured as shown in Figure 4b, and the experimental results confirmed the generated triboelectric charges of Q_1 and Q_2 and its co-accumulation charges of Q_1-Q_2 . In this case, the amount of transfer charges Q_1 and Q_2 together plays an essential role in enabling a high energy output of the TENG.

Since the transfer charges of the TENG are mainly influenced by the structural parameters, such as the surface

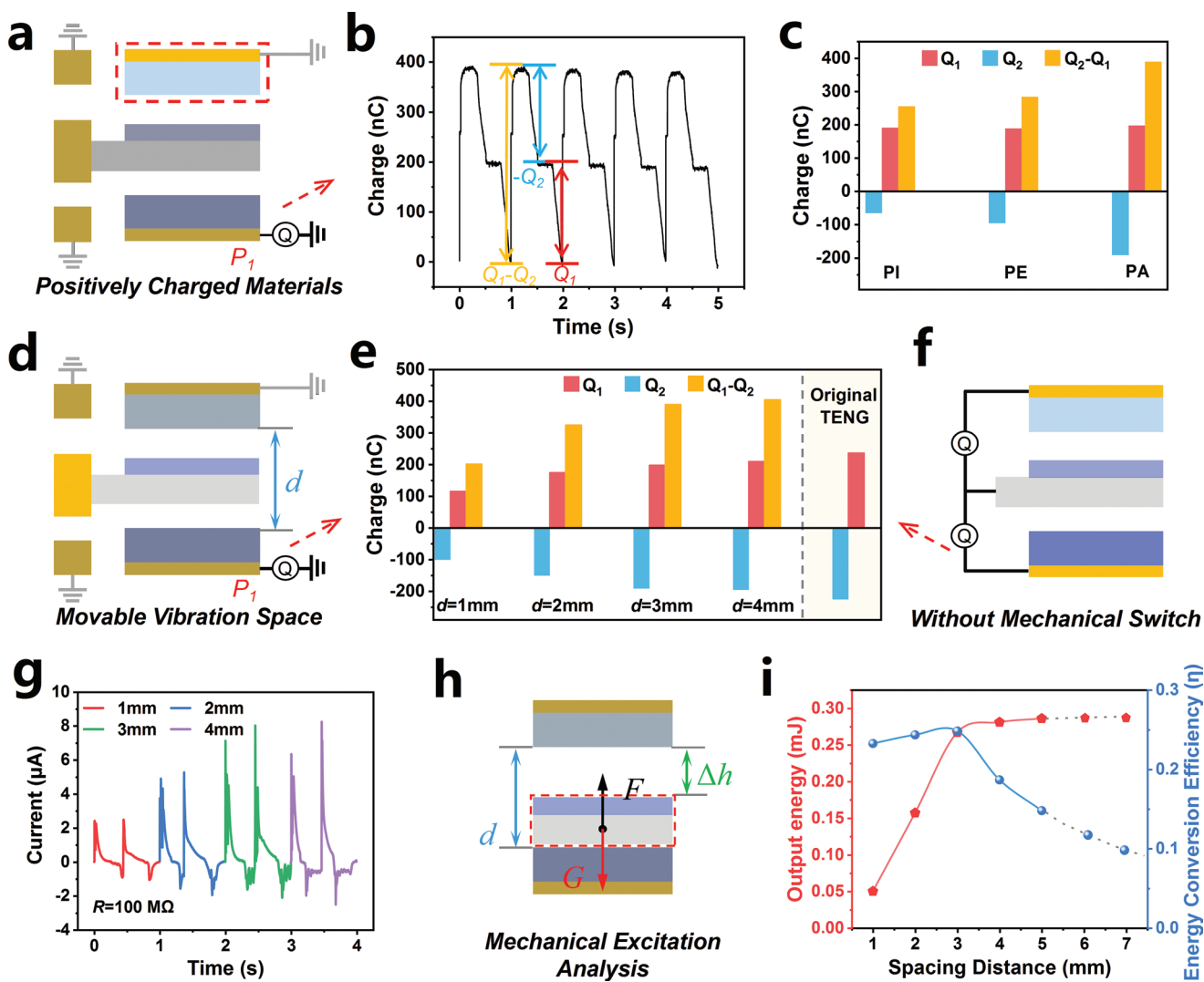


Figure 4. Structural parameters optimization of the TENG. a) Schematic illustration of the output charge measurement for various positively charged materials under the “4-Port” method. b) The measured transfer charge by PA as positively charged material. c) The counted Q_1 , Q_2 , and Q_1-Q_2 with various positively charged materials. d) Schematic illustration of the output charge measurement for various movable vibration spaces under the “4-Port” method, and e) its counted Q_1 , Q_2 , and Q_1-Q_2 . f) Schematic illustration of the output charge measurement for TENG without mechanical switch. g) The measured output current for an external load resistance of 100 M Ω with various movable vibration spaces. h) Schematic illustration of the mechanical excitation analysis for the movable layer. i) The output energy and energy conversion efficiency under various movable vibration spaces.

charge density within the triboelectric materials and overall vibration space provided for contact separation, which should be optimized, respectively. For the triboelectric materials, PTFE is considered the most triboelectric negatively charged material that can be paired with steel to achieve a maximum Q_2 , while a more positively charged material in top fixed layer paired with PTFE needs to be investigated to obtain the maximum Q_1 . Hence, the TENG was designed into different positively charged materials such as polyethylene, polyimide, and PA with the same thickness. Based on the measured transferred charge (Figure S6 in the Supporting Information), the counted Q_1 , Q_2 , and Q_1-Q_2 are plotted in Figure 4c. Obviously, the different materials introduced mainly lead to a variation in the Q_1 , which reflects their ability to donate electrons. In particular, the employed PA exhibits maximum charge transfer with a maximum Q_1 of 198 nC, thus it can be

considered as the optimum material to achieve higher output performance.

On the other hand, the TENG was designed into different overall vibration spaces to measure the transferred charge (Figure S7 in the Supporting Information), and the counted Q_1 , Q_2 , and Q_1-Q_2 are plotted in Figure 4e. From the experimental results, the transferred charge of Q_1 and Q_2 increases with the vibration space in the 1–3 mm, but it becomes saturated over the further increment, and eventually becomes a maximum Q_1-Q_2 of 405 nC at 4 mm. This behavior can be explained through the working mechanism of contact–separation TENG that increasing the separation of TENG leads to an increase in a potential difference between the triboelectric layers, and then plateaus after a threshold separation. Such a tendency will exist in an optimum separation distance where the negative charges of triboelectric layer are fully screened by the opposite charges

from only one electrode. Explainably, the practical distance that is less than the optimum separation will cause the reduction of the transferred charge, and any further separations exceeding the optimum distance will not promote the charge quantity, thus resulting in the transfer charge saturation after a higher separation distance. As a comparison, Figure 4f illustrates the original TENG without mechanical switch, i.e., the pairs of PTFE and PA, PTFE and steel, respectively. The output charges were measured under the maximum separation distance (Figure S8 in the Supporting Information), and the experimental results show that the original TENGs based on the above-mentioned two combinations have maximum transfer charges of 237 and 225 nC, respectively. Both of these values are larger than the Q_1 and Q_2 measured in Figure 4e. The reason is that the designed TENG may be affected by a large parasitic capacitance due to the multilayered structure in cooperation,^[57] resulting in a fact that generated triboelectric charge not being fully transferred through the external load.

Furthermore, energy conversion efficiency is a key parameter to evaluate the output performance of TENG in terms of both energy harvesting and utilization. This parameter can be usually regarded as the ability to convert external mechanical excitation into electrical output. In this case, the energy conversion efficiency η can be defined as

$$\eta = \frac{E_{\text{out}}}{E_{\text{in}}} \quad (4)$$

where E_{in} is the occurred external mechanical excitation and E_{out} is the generated energy of TENG. To explore the overall output energy E_{out} for TENG, the output current into different vibration spaces was measured by connecting to external loads resistance of 100 M Ω , as shown in Figure 4g. Based on the experimental results, the V - Q plots (Figure S9 in Supporting Information) were graphed and the output energies E_{out} were further counted in Figure 4i. It can be seen that the E_{out} increases linearly with d growing from 1 to 3 mm, and gradually reaches the saturation status with a maximum $E_{\text{out}} = 0.29$ mJ at 4 mm. The observed increment in E_{out} is intrinsically attributed to an increased transfer charge as mentioned above.

For mechanical excitation, the movable layer in vibration space is focused on input energy analysis, as shown in the inset of Figure 4h. The movement of the movable layer requires sufficient mechanical excitation for a full contact separation process with the top and bottom layers. Based on the mechanical energy conservation, we assume that the required kinetic energy is fully converted into potential energy in one cycle, i.e., the minimum mechanical excitation to ensure the normal operation of the TENG. Thus, the required mechanical excitation E_{in} can be evaluated by potential energy at different vibration spaces, which is expressed as follows

$$E_{\text{in}} = G \cdot \Delta h \quad (5)$$

where G is the gravity of the movable layer, and $G = mg$. m is the mass of the movable layer, g is the gravitational acceleration ($g = 9.8$ m s⁻²). Δh is the effective moving distance in the whole vibration space of d . The mass of the movable layer is shown in Figure S10 in the Supporting Information, where the detailed

numerical calculation of the energy conversion efficiency is also presented. Therefore, the efficiency η is further obtained under various movable vibration spaces, as shown in Figure 4i. The relationship between η and d can be divided into two parts, in which η maintains well efficiency with increasing d from 1 to 3 mm, while decreasing rapidly from $d = 4$ mm, such that the highest η of 0.25 is obtained at 3 mm. It can be concluded that the TENG at 3 mm vibration space is close to the optimum separation value that can be selected to achieve optimum energy conversion efficiency with high output energy, simultaneously, where the optimized structure is highly favorable to ambient vibration adaptation and high power demand in practical engineering applications.

2.4. Dual-Channel Power Management Circuit Combination

Based on the excellent output performance of TENG, a dual-channel PMC with only rectifier diodes is designed for external loads. The structure and working mechanism of the simple PMC are shown in Figure 5a and Figure S11 in the Supporting Information. In this case, the ID current and CD current generated by TENG can be finely separated into two DC outputs. With the dual-channel PMC connected to the TENG, the measured output currents of each channel are shown in Figure 5b,c, respectively.

For an in-depth comparison of the output characteristics between the ID-channel and the CD-channel, the output voltage and current of each channel were measured under varied external load resistances and the peak values of voltage and current are shown in Figure 5d,e. Under the CD-channel, the output voltage rises gradually from 0 to 225 V with the increased load resistance from 1 k Ω to 1 G Ω , while the output current falls from 3.7 μ A to 0, exhibiting a reverse trend. But for the ID-channel, a stable output voltage of about 800 V can be maintained at different resistances, while the output current increases rapidly with decreased load resistance, reaching a large current of 0.78 A with a resistance of 1 k Ω . Since the mechanical switch is introduced to keep the established potential to a maximum value, whose output voltages are independent of the load resistance. Thus, a smaller load can be powered by a larger current.

Meanwhile, the output powers for dual-channel are also obtained with varied external load resistances as shown in Figure 5f. Specifically, the output power of CD-channel rises gradually with the increased load resistance and then becomes a downtrend, and a maximum output power of 0.35 mW can be reached at a high resistance load of 1 M Ω . Such a tendency is consistent with the output characteristics of conventional TENG. Unlike the above output characteristic, the output power of the ID-channel exhibits a dramatic rise with the decreased load resistance, and eventually reaches a giant output power of 616 W at 1 k Ω , which exceeds 10⁶ times more than the CD-channel. Benefiting from the mechanical switch trigger mechanism, the ID-channel features close to zero internal resistance that enables a high-power supply for low-impedance loads, while the CD-channel is just suitable for high-impedance loads because of its intrinsic characteristic with large internal resistance.

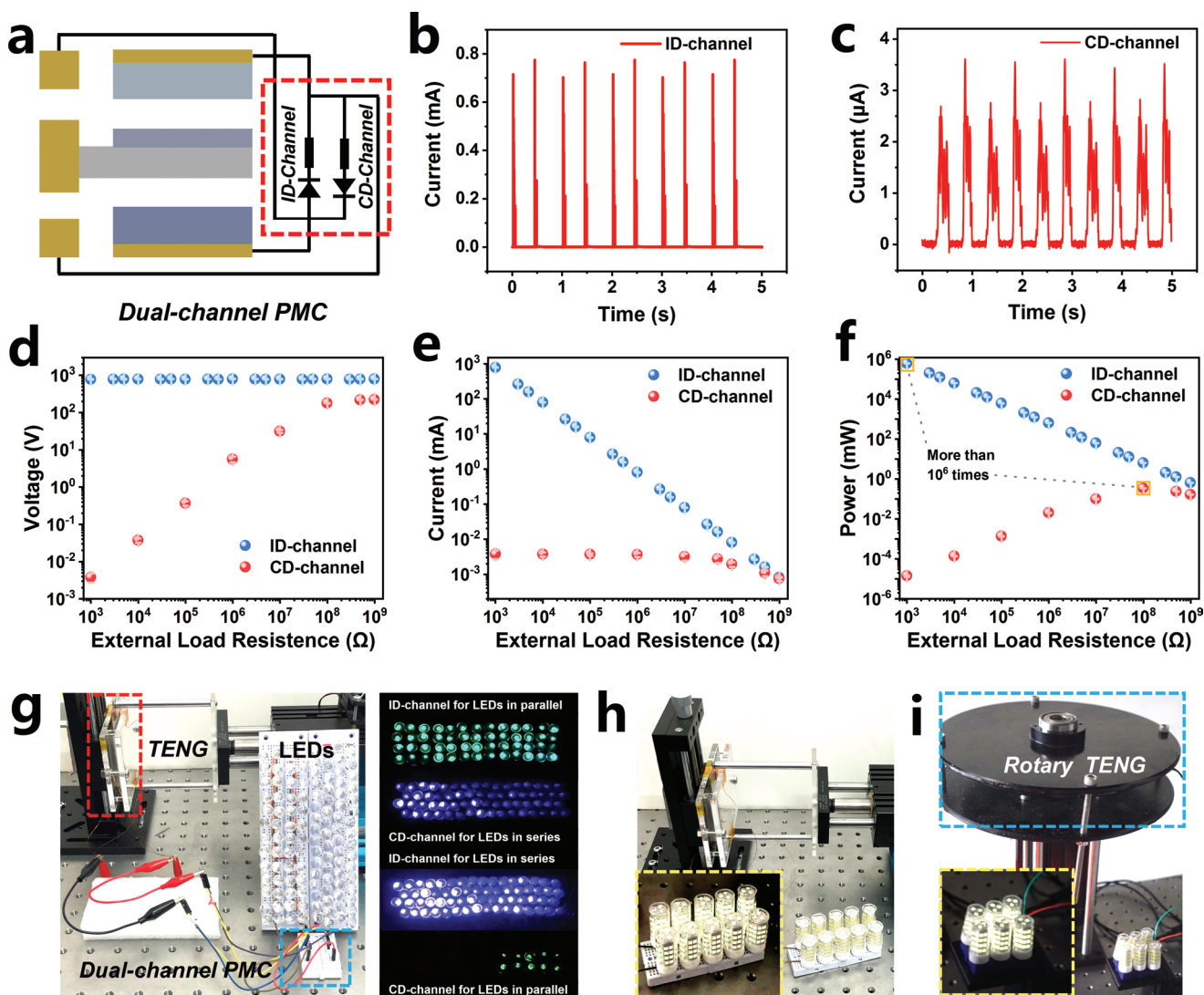


Figure 5. Dual-channel power management circuit combination for the TENG. a) Schematic illustration of the dual-channel power management circuit. The measured output current of the TENG in b) ID-channel and c) CD-channel with both external load resistance of 1 M Ω . Variations of d) output voltage, e) current, and f) peak power of the TENG in dual-channel depend on varied external load resistances. g) The energy supply capacity of the TENG in dual-channel for series and parallel connected LED arrays. Comparison of the power supply capacity for high-power lamps in parallel via h) our designed TENG and i) high-speed rotary TENG.

To further explore and compare the power supply capabilities of the two channels generated by TENG, the LED arrays were applied as external loads connected to the PMC for visual comparison. Specifically, 50 green LEDs were connected in parallel to the ID-channel, while 50 blue LEDs were connected in series to the CD-channel. Notably, the LEDs in parallel have low internal resistance, while the series form offers large internal resistance. Of course, the LEDs herein are high power (20 mA, 3 V) with a 10 mm diameter as shown in Figure 5g (the detailed circuit diagram is shown in Figure S12 in the Supporting Information). As the TENG was driven by a linear motor at a frequency of 1 Hz, both channels of the LED arrays can be illuminated, which confirms the power supply capability of the ID-channel for low-impedance loads in paralleled LED form. In addition, the LED loads were exchanged with each other and then connected to the channels, i.e., the blue LEDs in series

are connected to the ID-channel and the green LEDs in parallel are connected to the CD-channel. With the same power supply conditions as above, the ID-channel remains excellent for large impedance loads, but the CD-channel can only light ten LEDs, and more LEDs introduced will not be available. The verification process is further demonstrated in Movie S1 in the Supporting Information. Finally, Figure 5h illustrates ten commercial high-power lamps (50 W, 220 V) being introduced into the ID-channel in parallel, and all of them were illuminated by TENG. Additionally, the conventional TENG is referred for comparison with our designed TENG, while the rotary TENG has been regarded as the most high-output, high-efficiency, and sustainable energy supply in all prototypes of the conventional TENG modes. As a comparison, a rotary TENG as an example was utilized to illuminate six lamps in parallel, as shown in Figure 5i. However, such a large-sized conventional TENG

would be driven by a high speed with 400 rpm to generate the required giant output power. The comparison process is demonstrated in Movie S2 in the Supporting Information.

2.5. Vibration Sensor Construction and Demonstration

Figure 6a demonstrates an all-in-one sensing system combined with TENG and IR communication. Typically, IR LED is utilized as a transmitter paired with an IR receiver module to form a wireless communication system, which can transmit information by IR waves in the ambient medium. The IR LED introduced here as an external load and also features a wireless communication module, therefore, it is a promising way to combine the IR LED with the TENG together into a vibration sensor for further attempts. However, a reliable signal transmission based on IR communication over a long distance requires an adequate power supply to ensure effective signal transmission. In this regard, a commercial current power source instead of TENG was employed to drive an IR LED in order to investigate the transmission capability, and the generated IR intensity was collected simultaneously by an IR receiver module. Here, the IR intensity can be defined as

$$IR_{\text{intensity}} = \frac{V_{\text{CC}} - V_{\text{out}}}{V_{\text{CC}}} \times 100\% \quad (6)$$

where V_{CC} is the power supply voltage of the IR receiver as well as the reference voltage, V_{out} is the output analog signal from the IR receiver. Subsequently, the dependence of the received IR intensity with varied forward currents passing through the IR LED was measured under a communication distance of 50 cm, as shown in Figure 6b, and the inset shows the V - I plot of the IR LED. From the experimental results, it can be found that as the forward current increases, the value of V_{out} increases accordingly to exhibit a better IR intensity. Notably, a large current of mA-level is required for the IR LED to maintain well communication.

Given such features, the IR LED was connected to the TENG for functional verification, and an electromagnetic shaker is operated as an excitation source. Take the excitation of vibration frequency with 10 Hz as an example, the vibration sensor was successfully driven to enable communication with a distance of 50 cm. The generated signal by the TENG and the output signal feedback from the IR receiver as shown in Figure 6c,d, respectively. It can be observed that the ID-channel of the TENG can supply sufficient energy for the IR LED, and simultaneously transmit the output properties completely with a peak IR intensity of 45%. In contrast, the IR LED was also driven by the conventional contact-separation TENG which provided only a weak IR intensity of 2% as well as being available over short distances of 10 cm (the detailed verification is shown in Figure S13 in the Supporting Information). Therefore, the unique combination of our designed TENG and IR LED can enable an all-in-one vibration sensor to realize stable signal transmissions. Specifically, the TENG generates a giant ID current under the periodic contact-separation that can power the IR LED to ensure wireless communication. On the other hand, the transmitted pulse signal can also feedback the vibration frequency information of the

current vibration excitation. With the features of self-powered, vibration sensing, and wireless communication, the all-in-one vibration sensor opens up novel pathways for vibration state online monitoring.

For engineering applications in the electrical field, a functional IR LED is also necessary to be selected that fully utilizes the energy generated by the TENG to establish reliable communication. Therefore, the intrinsic parameters of the LED were systematically investigated in terms of central wavelength λ and diameter Φ . Figure 6e illustrates the dependence of IR intensity with communication distance for IR LED with various parameters. Compared to $\lambda = 940$ nm, the IR LED with $\lambda = 850$ nm enables farther communication under the same excitation, this is because the shorter wavelength of $\lambda = 850$ nm with higher frequency demonstrates a better penetration ability in the ambient medium. Meanwhile, it can be found that after the diameter of IR LED in 850 nm increases from $\Phi = 5$ mm to $\Phi = 10$ mm, the IR intensity increases significantly, which results in stronger signals and reliable transmission at a communication distance of 200 cm or even farther distance. The attenuation of the IR intensity over longer distances can be fitted out via a one-phase exponential decay function as indicated in Figure 6e. The estimated results show that the longest communication distance could be up to 1000 cm. Hence, the 850 nm IR LED with $\Phi = 10$ mm is an optimum choice for a transmitter of vibration sensor in practical applications. Table S1 in the Supporting Information illustrates the comparison with previously reported TENG-based wireless communication sensor systems. In comparison, the TENG in this work is designed with a compact sandwich structure, which can be easily triggered by microvibration of 3 mm. Moreover, the whole sensor avoids extra-long pre-charging time for the external signal processing module that enables real-time signal transmission. Furthermore, the IR communication perfectly eliminates the electromagnetic interference of RF-based technology while at near-electromagnetic fields in power grid. More importantly, the mechanical switch-triggered TENG with lighter weight and smaller size provides giant power for IR LEDs to deliver long-distance wireless transmission, which enables the sensor to be installed into the inside even bottom of the large equipment for transmitting the invisible or imperceptible abnormal signal in the complex interior structure. The all-in-one vibration sensor represents a breakthrough in terms of practicality for online monitoring applications in electrical equipment.

Finally, the vibration sensor is integrated with microcontroller unit (MCU) and mobile phone platform to establish a fully wireless vibration online monitoring system, as shown in Figure 6f. In the platform, The ESP-32 MCU combined with the IR receiver forms a repeater to further signal conversion and transmission. Meanwhile, a graphical user interface was designed on the mobile phone for the vibration states visualization. Additionally, an electromagnetic shaker is operated as an excitation source to simulate the vibration on electrical equipment. The vibration frequency can be regulated via a signals programmer involving a signal controller and a power amplifier. The workflow of the fully wireless communication network is illustrated in Figure 6g. Once the vibration sensor is triggered, the generated state information will be transmitted from IR LED to the repeater, whose MCU performs the analog

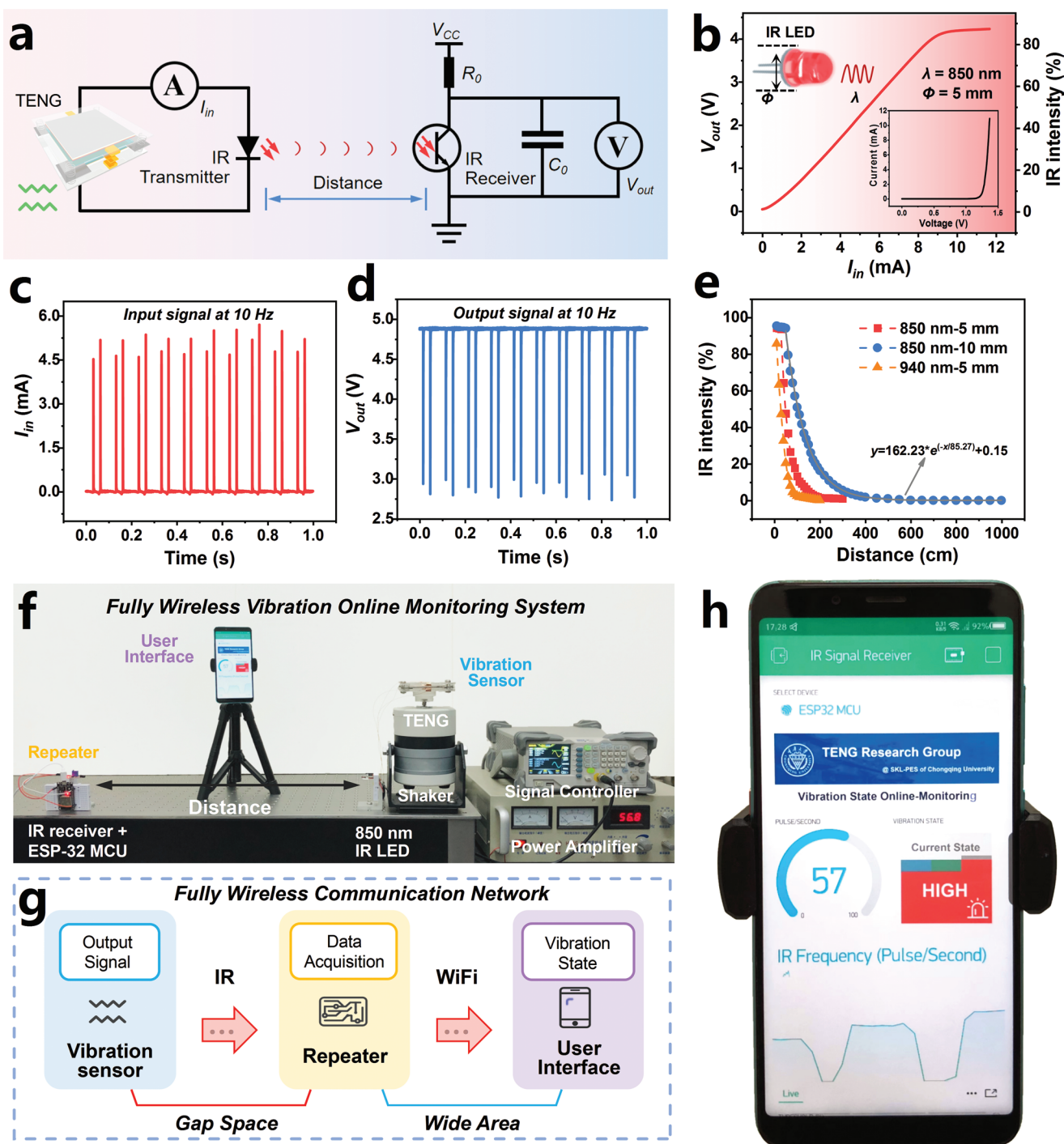


Figure 6. Demonstration of the all-in-one vibration sensor for fully wireless vibration state online monitoring. a) Schematic illustration of an all-in-one sensing system combined by TENG and IR communication. b) The received IR intensity at a 50 cm communication distance with varied currents pass through the IR LED. c) The generated signal by the vibration sensor and d) the output signal feedback from the IR receiver (under a communication distance of 50 cm). e) Dependence of IR intensity with communication distance for IR LED with various parameters. f) Photograph of the fully wireless vibration online monitoring system. g) The workflow diagram of the fully wireless communication network. h) Demonstration of vibration state online-monitoring visualized by a mobile phone.

to-digital conversion and sends the data to the phone via the built-in WiFi module. In this case, IR communication enables in situ vibration online monitoring in a gap space that cannot be covered by traditional communication, while the WiFi-based

network allows the vibration data to be sensed over a wide area. Thus, the established fully wireless communication network realizes complementary advantages to each other for a broad interaction in eIoT.

For any triggered vibration excitation, the vibration data can be transmitted quickly in the wireless communication network, and eventually visualized on the mobile phone (Figure 6h and Movie S3 in the Supporting Information). Based on the vibration data, the current frequency and frequency distribution can be checked by users. In this demonstration, abnormal vibrations with three different frequencies are used to drive the sensor, and the experimental results show that the obtained frequencies are consistent with the excitation frequencies (Table S2 in the Supporting Information). Benefiting from the true feedback of the vibration excitation, the pulse statistics via the TENG output signal provide a promising method to obtain accurate frequency information about the actual situation. Also, the integrated IR communication makes the all-in-one sensor become more fast and more sensitive in the vibration information interaction. As an extension, the current vibration state can also be evaluated according to defined frequency thresholds. The above demonstration proves the potential of a fully wireless vibration online monitoring system applied to vibration frequency-based state monitoring in a convenient and reliable manner. The TENG-based all-in-one sensing system can be considered a flexible, effective, and low-cost method for the distributed in situ online monitoring of most key electrical equipment such as the typical scenarios of hydraulic turbine, transformer, gas-insulated switchgear, and transmission line. The whole system also provides a novel perspective for long-term equipment health condition monitoring, whose abnormal vibrations can be further utilized for in-depth evaluation of equipment defect issues. Moving forward, the miniaturization and integration of sensors is an essential trend for the deep construction of distributed sensors in the future smart grid, which is also a technical challenge to make it lighter, easily deployed, and well-networked for the universal vibration monitoring of various electrical equipment, resulting in a new set of miniature intelligent sensing technology solutions for IoT construction.

3. Conclusion

In summary, an all-in-one vibration sensor integrated by TENG and IR LED is proposed for online monitoring of the vibration frequency state. The TENG consists of a three-layered sandwich structure with integrated mechanical switches, which can be triggered to release co-accumulated charges as the middle movable layer moves between the top and bottom fixed layers periodically. Based on structural design, the output characteristics of ID mode maintain stable maximum output energy for different external resistances and are even independent of frequency. Moreover, the “4-port” method was applied to verify the co-accumulated charges of Q_1 – Q_2 , as well as to optimize the structural parameters of TENG in terms of paired triboelectric materials and vibration space. The experimental results have given an optimum energy conversion efficiency η of 0.25 with the coupled PTFE and PA in a microvibration space of 3 mm. For the external circuit of the optimized TENG, a dual-channel PMC was designed to enable the DC output of the individual ID-channel and CD-channel. The ID-channel generates giant instantaneous power of 616 W at small resistance of 1 k Ω that successfully illuminates parallel-connected

LED arrays and 50 W high-power lamps. This unique output characteristic makes it with lighter weight and smaller size compared with previous TENG under the same output. Finally, an 850 nm IR LED with $\Phi = 10$ mm as a transmitter is connected to TENG to form an all-in-one vibration sensor. Under the simulated vibration excitation, the ID output generated from the sensor provides a giant power supply to the IR LED for distance communication up to 1000 cm, and simultaneously serves as a sensing signal for the vibration state. Such long-distance signal transmission based on IR communication as well as the features of electromagnetic interference-free and nonmetal shielding represents a breakthrough for the traditional RF technology limited in the power field. Integrated IR receiver and MCU-based repeater as well as mobile phone platform into the sensor to demonstrate a fully wireless vibration online monitoring system, enabling a visual function for vibration frequency monitoring and predefined state evaluation over a wide area. The proposed work provides a high-power output and high-efficiency method to extend the TENG technology into a broad range of power supplies, and more importantly, the combined all-in-one vibration sensor offers considerable potential to be deployed into most high-voltage electrical equipment and even its interior scenes toward the challenge of in situ monitoring with abnormal vibration and further intrinsic defect analysis.

4. Experimental Section

Modification of PTFE and PA Film: The PTFE films (10 and 100 μm in thickness) and PA film (100 μm in thickness) were placed in an inductively coupled plasma instrument (STS LPX ASE-SR) chamber, and etched by 400 W, 40 kHz air plasma for 10 and 5 min, respectively. After that, the treated samples were ultrasonically cleaned with deionized water and ethanol successively, then dried in a drying oven before use.

Fabrication of TENG: The TENG mainly consisted of two components: two fixed layers and a movable layer.

For the two fixed layers, a 2 mm thick acrylic sheet was cut by a laser cutter (Universal Laser System PLS6.75) as substrates with dimensions of 90 mm \times 90 mm. The 60 mm \times 60 mm sponge layer (1 mm in thickness) and copper foil (50 μm in thickness) were attached to the center of the acrylic substrate, sequentially. Next, the PA film (100 μm in thickness) and PTFE film (100 μm in thickness) of the same size as above were attached to the surface of the copper foil as the top and bottom fixed layers, respectively. Meanwhile, 1 mm \times 1 mm copper foil with an acrylic pad was attached to the edge of the acrylic substrate as mechanical contact.

For the movable layer, a 0.5 mm thick steel chip was cut into a square with a major area of 60 mm \times 60 mm, while mechanical contact was extended at one side and also with four legs in corners. Next, the PTFE film (10 μm in thickness) of the same size was attached to the upper surface of the steel. Finally, four sets of steel springs (12 mm \times 12 mm \times 5 mm) were fixed between the fixed and moveable layers.

Experimental Measurements: A field-emission SEM (Hitachi SU8010) was used to characterize the surface nanostructures of etched PTFE and PA film. For the evaluation of basic output performance, the periodic contact–separation process TENG was driven by a linear motor (LinMot H01-37 \times 166/280) in quantified measurement. For the vibration sensing monitoring, the TENG was mounted on an electromagnetic shaker (HEV-50) driven by an amplifier (HEA-50) and signal controller (RIGOL DG1022Z) with a sinusoidal signal output. The typical electrical signals of the TENG were measured by a programmable electrometer (Keithley 6514). The high-sensitivity acquisition card (National Instrument NI 9220, 16-channel voltage measurement module, ± 10 V) was used to

measure high-frequency giant current from the equation $I = V/R$. The measurement signals were visualized in a high-speed data acquisition system under LabView 2016. An oscilloscope (TELEDYNE LECROY, WaveRunner 8054) was used to measure the voltage higher than 200 V. The DC power supply (TN-XXZ02) was adopted as the current source for testing the IR LED.

Demonstration: The fully wireless vibration online monitoring system was integrated with a vibration sensor, a repeater, and a mobile phone, which worked together to enable fully wireless communication in IR and WiFi modes. An IR LED (wavelength: 850 nm, diameter: 10 mm) as a transmitter was integrated into TENG to form a vibration sensor. The repeater consisted of an IR receiver module and an ESP-32 MCU (sampling frequency of 100 kHz, 2.4 GHz Wi-Fi module). The graphical user interface (GUI) on the mobile phone for vibration state visualization was built on Blynk, an open-source IoT platform.

Supporting Information

Supporting Information is available from the Wiley Online Library or from the author.

Acknowledgements

H.W. and Z.W. contributed equally to this work. This work was supported by the National Natural Science Foundation of China (grant no. 52007019).

Conflict of Interest

The authors declare no conflict of interest.

Data Availability Statement

The data that support the findings of this study are available from the corresponding author upon reasonable request.

Keywords

all-in-one sensing system, IR wireless communication, mechanical switches, triboelectric nanogenerators, vibration sensors

Received: January 5, 2023

Revised: February 8, 2023

Published online:

- [1] A. D. Maynard, *Nat. Nanotechnol.* **2015**, *10*, 1005.
- [2] G. Dileep, *Renewable Energy* **2020**, *146*, 2589.
- [3] M. B. Mollah, J. Zhao, D. Niyato, K. Y. Lam, X. Zhang, A. M. Y. M. Ghias, L. H. Koh, L. Yang, *IEEE Internet Things J.* **2021**, *8*, 18.
- [4] H. Wang, J. Wang, K. Yao, J. Fu, X. Xia, R. Zhang, J. Li, G. Xu, L. Wang, J. Yang, J. Lai, Y. Dai, Z. Zhang, A. Li, Y. Zhu, X. Yu, Z. L. Wang, Y. Zi, *Sci. Adv.* **2021**, *7*, eabi6751.
- [5] Z. Ren, X. Liang, D. Liu, X. Li, J. Ping, Z. Wang, Z. L. Wang, *Adv. Energy Mater.* **2021**, *11*, 2101116.
- [6] P. Moutis, O. Alizadeh-Mousavi, *IEEE Trans. Power Delivery* **2021**, *36*, 1952.

- [7] Y. Shi, S. Ji, F. Zhang, Y. Dang, L. Zhu, *IEEE Trans. Power Delivery* **2021**, *36*, 2164.
- [8] Q. Chai, Y. Luo, J. Ren, J. Zhang, J. Yang, L. Yuan, G. Peng, *Opt. Eng.* **2019**, *58*, 072007.
- [9] X. Tang, W. Hou, Q. Zheng, L. Fang, R. Zhu, L. Zheng, *Nano Energy* **2022**, *99*, 107412.
- [10] Z. Yuan, X. W. , X. Jin, Y. Sun, Z. Wu, Z. L. Wang, *Mater. Today Energy* **2021**, *22*, 100848.
- [11] Z. Wang, A. Sharma, *J. Intell. Syst.* **2021**, *30*, 677.
- [12] A. Zollanvari, K. Kunanbayev, S. Akhavan Bitaghsir, M. Bagheri, *IEEE Trans. Instrum. Meas.* **2021**, *70*, 9205841.
- [13] Z. Long, X. Huang, J. Jia, Y. Zhu, C. Wen, *Sensors* **2018**, *18*, 2397.
- [14] H. Wu, J. Wang, Z. Wu, S. Kang, X. Wei, H. Wang, H. Luo, L. Yang, R. Liao, Z. L. Wang, *Adv. Energy Mater.* **2022**, *12*, 2103654.
- [15] F. Zhang, S. Ji, H. Ma, T. K. Saha, *IEEE Trans. Power Delivery* **2020**, *35*, 1285.
- [16] Z. Zhang, J. Li, Y. Song, Y. Sun, X. Zhang, Y. Hu, R. Guo, X. Han, *IEEE Trans. Power Delivery* **2022**, *37*, 1937.
- [17] R. Haight, W. Haensch, D. Friedman, *Science* **2016**, *353*, 124.
- [18] W. Q. Qin, G. M. Ma, M. Zhang, Y. Wang, J. Jiang, H. Zhou, X. Wang, C. Yan, *IEEE Trans. Ind. Electron.* **2022**, *69*, 10625.
- [19] F. Fan, Z. Tian, Z. L. Wang, *Nano Energy* **2012**, *1*, 328.
- [20] Z. L. Wang, *Mater. Today* **2017**, *20*, 74.
- [21] Z. L. Wang, *Adv. Energy Mater.* **2020**, *10*, 2000137.
- [22] H. Guo, X. Pu, J. Chen, Y. Meng, M.-H. Yeh, G. Liu, Q. Tang, B. Chen, D. Liu, S. Qi, C. Wu, C. Hu, J. Wang, Z. L. Wang, *Sci. Rob.* **2018**, *3*, 2516.
- [23] Q. Su, Q. Zou, Y. Li, Y. Chen, S. Y. Teng, J. T. Kelleher, R. Nith, P. Cheng, N. Li, W. Liu, S. Dai, Y. Liu, A. Mazursky, J. Xu, L. Jin, P. Lopes, S. Wang, *Sci. Adv.* **2021**, *7*, eabi4563.
- [24] Z. Zhao, L. Zhou, S. Li, D. Liu, Y. Li, Y. Gao, Y. Liu, Y. Dai, J. Wang, Z. L. Wang, *Nat. Commun.* **2021**, *12*, 4686.
- [25] S. Yong, J. Wang, L. Yang, H. Wang, H. Luo, R. Liao, Z. L. Wang, *Adv. Energy Mater.* **2021**, *11*, 2101194.
- [26] H. Wu, W. He, C. Shan, Z. Wang, S. Fu, Q. Tang, H. Guo, Y. Du, W. Liu, C. Hu, *Adv. Mater.* **2022**, *34*, 2109918.
- [27] B. Cao, P. Wang, P. Rui, X. Wei, Z. Wang, Y. Yang, X. Tu, C. Chen, Z. Wang, Z. Yang, T. Jiang, J. Cheng, Z. L. Wang, *Adv. Energy Mater.* **2022**, *12*, 2202627.
- [28] Y. Zi, S. Niu, J. Wang, Z. Wen, W. Tang, Z. L. Wang, *Nat. Commun.* **2015**, *6*, 8376.
- [29] Y. Zi, J. Wang, S. Wang, S. Li, Z. Wen, H. Guo, Z. L. Wang, *Nat. Commun.* **2016**, *7*, 10987.
- [30] T. Hu, H. Wang, W. Harmon, D. Bamgboje, Z. L. Wang, *IEEE Trans. Power Electron.* **2022**, *37*, 9850.
- [31] W. Harmon, D. Bamgboje, H. Guo, T. Hu, Z. L. Wang, *Nano Energy* **2020**, *71*, 104642.
- [32] S. Niu, X. Wang, F. Yi, Y. S. Zhou, Z. L. Wang, *Nat. Commun.* **2015**, *6*, 8975.
- [33] W. Liu, Z. Wang, G. Wang, Q. Zeng, W. He, L. Liu, X. Wang, Y. Xi, H. Guo, C. Hu, Z. L. Wang, *Nat. Commun.* **2020**, *11*, 1883.
- [34] Z. Wang, W. Liu, W. He, H. Guo, L. Long, Y. Xi, X. Wang, A. Liu, C. Hu, *Joule* **2021**, *5*, 441.
- [35] H. F. Qin, G. Cheng, Y. Zi, G. Gu, B. Zhang, W. Shang, F. Yang, J. Yang, Z. Du, Z. L. Wang, *Adv. Funct. Mater.* **2018**, *28*, 1805216.
- [36] H. Wu, S. Wang, Z. Wang, Y. Zi, *Nat. Commun.* **2021**, *12*, 5470.
- [37] G. Cheng, Z. H. Lin, L. Lin, Z. L. Du, Z. L. Wang, *ACS Nano* **2013**, *7*, 7383.
- [38] Y. Song, J. Min, Y. Yu, H. Wang, Y. Yang, H. Zhang, W. Gao, *Sci. Adv.* **2020**, *6*, eaay9842.
- [39] X. Zhao, G. Wei, X. Li, Y. Qin, D. Xu, W. Tang, H. Yin, X. Wei, L. Jia, *Nano Energy* **2017**, *34*, 549.
- [40] X. Zhao, G. Wei, X. Li, Y. Qin, D. Xu, W. Tang, H. Yin, X. Wei, L. Jia, *Nano Energy* **2017**, *34*, 549.

- [41] A. Pospischil, M. Humer, M. M. Furchi, D. Bachmann, R. Guider, T. Fromherz, T. Mueller, *Nat. Photonics* **2013**, *7*, 892.
- [42] R. Lin, X. Liu, G. Zhou, Z. Qian, X. Cui, P. Tian, *Adv. Opt. Mater.* **2021**, *9*, 2002211.
- [43] H. Hu, L. K. Oxenløwe, *Nanophotonics* **2021**, *10*, 1367.
- [44] W. Ding, C. Wu, Y. Zi, H. Zou, J. Wang, J. Cheng, A. C. Wang, Z. L. Wang, *Nano Energy* **2018**, *47*, 566.
- [45] M. Casalino, U. Sassi, I. Goykhman, A. Eiden, E. Lidorikis, S. Milana, D. De Fazio, F. Tomarchio, M. Iodice, G. Coppola, A. C. Ferrari, *ACS Nano* **2017**, *11*, 10955.
- [46] M. Yang, Q. Han, X. Liu, J. Han, Y. Zhao, L. He, J. Gou, Z. Wu, X. Wang, J. Wang, *Adv. Funct. Mater.* **2020**, *30*, 1909659.
- [47] Z. Wang, Y. Jin, C. Lu, J. Wang, Z. Song, X. Yang, Y. Cao, Y. Zi, Z. L. Wang, W. Ding, *Energy Environ. Sci.* **2022**, *15*, 2983.
- [48] P. Pennacchi, P. Borghesani, S. Chatterton, *Mech. Syst. Signal Process.* **2015**, *60*, 375.
- [49] B. Xu, D. Chen, H. Zhang, C. Li, J. Zhou, *J. Sound Vib.* **2018**, *435*, 74.
- [50] K. Hong, H. Huang, J. Zhou, *IEEE Trans. Power Delivery* **2015**, *30*, 1735.
- [51] Y. Shi, S. Ji, F. Zhang, Y. Dang, L. Zhu, *IEEE Trans. Power Delivery* **2021**, *36*, 2164.
- [52] Y. Yang, S. Ma, J. Wu, B. Jia, W. Li, X. Luo, *Sensors* **2019**, *19*, 1949.
- [53] Y. Zhong, J. Hao, R. Liao, X. Wang, X. Jiang, F. Wang, *High Voltage* **2021**, *6*, 531.
- [54] X. Huang, L. Zhao, G. Chen, *Sensors* **2016**, *16*, 1657.
- [55] Q. Yan, C. Zhou, X. Feng, C. Deng, W. Hu, Y. Xu, *Photonic Sens.* **2022**, *12*, 220310.
- [56] C. Xu, Y. Zi, A. C. Wang, H. Zou, Y. Dai, X. He, P. Wang, Y. C. Wang, P. Feng, D. Li, Z. L. Wang, *Adv. Mater.* **2018**, *30*, 1706790.
- [57] J. Peng, S. D. Kang, G. J. Snyder, *Sci. Adv.* **2017**, *12*, 8576.
- [58] S. S. K. Mallineni, Y. Dong, H. Behlow, A. M. Rao, R. Podila, *Adv. Energy Mater.* **2018**, *8*, 1702736.